IEEE Access
Multidisciplinary | Rapid Review | Open Access Journal

IEEE POWER & ENERGY SOCIETY SECTION

Received 30 October 2023, accepted 17 November 2023, date of publication 20 November 2023,
date of current version 28 November 2023.

Digital Object Identifier 10.1109/ACCESS.2023.3335133

RESEARCH ARTICLE

Optimization of Wind Power Curtailment by OPF in Hybrid AC/VSC-HVDC Systems With DC Voltage Constraints

SANGWON KIM, (Member, IEEE)
Department of Electrical, Electronic and Computer Engineering, University of Ulsan, Ulsan 44610, South Korea
e-mail: angwon22@ulsan.ac.kr

This work was supported by the National Research Foundation of Korea (NRF) grant funded by the Korean Government (MSIT) under Grant RS-2022-00165574.

ABSTRACT This paper proposes an optimization method for wind power output curtailment based on optimal power flow (OPF) analysis. The wind curtailment ratio is incorporated as a controllable variable in the OPF formulation. A voltage-source converter based high-voltage direct current (VSC-HVDC) system is installed in a power system model considering large-scale wind farm integration. Inertia emulation control (IEC) is implemented for the VSC-HVDC system. When a disturbance occurs, the VSC-HVDC system can participate in the AC grid frequency stabilization by supplying active power. However, the utilization of the active power in the VSC-HVDC system results in DC grid voltage fluctuation. This fluctuation can be reduced if the IEC frequency control can be replaced by wind-side frequency regulation. However, wind-based frequency control requires wind output suppression to obtain the reserve capacity. This is undesirable for minimizing the fuel cost objective function. In this context, the novel point of this paper is to determine the optimal wind output curtailment considering both the fuel cost objective function and the DC voltage constraints by the OPF analysis. Considering the DC voltage reference deviation occurred by the IEC, the deviation range of the DC voltage reference is limited as an inequality constraint to prevent infeasible DC voltage fluctuations. Based on this approach, the advantage of wind output suppression can be analyzed from the DC voltage perspective. Sensitivity analysis on the DC voltage constraints, wind power plant capacity, and VSC-HVDC system capacity is performed to prove the effectiveness of the proposed method.

INDEX TERMS DC voltage constraint, VSC-HVDC, optimal power flow, primary frequency support, wind power curtailment.

I. INTRODUCTION

A. RESEARCH BACKGROUND

The global role of renewable energy sources (RES) including photovoltaics and wind generation is expanding for more sustainable power systems. The effectiveness of high-voltage direct current systems with voltage-source converters (VSC-HVDC) have been assessed for large-scale wind power plants (WPPs) [1], [2], [3]. Compared to line-commutated conventional HVDC systems, VSC-HVDC systems are more appropriate for systems with high fluctuations of AC bus voltages and wind power output owing to the independent active and reactive power controllability [4], [5], [6].

Meanwhile, reduced power system inertia is a critical problem since power-electronics-based RES generation and VSC-HVDC do not have any inertial response [7]. For example, the increased frequency deviation and rate of change of frequency (ROCOF) after a disturbance leads to generator disconnection and load-shedding [8], [9]. In order to solve this phenomenon, frequency support based on a VSC-HVDC system can be implemented by utilizing the energy from the DC grid side. However, this has the risk of DC grid voltage fluctuation. A large DC voltage deviation can lead to not only the unstable terminal bus voltage in AC grid side [10], but also a negative impact on the DC grid protection relay [11].

The associate editor coordinating the review of this manuscript and approving it for publication was Yifan Zhou.

If WPPs can provide a frequency support service, the risk of DC voltage fluctuation can be avoided. Instead, the wind power output should be curtailed to secure wind-side reserve capacity. This deloaded wind operation is beneficial for suppressing DC voltage fluctuation. Nevertheless, this wind output suppression results in increased fuel costs for the synchronous generators. The output suppression is not required if DC voltage can be controlled within a feasible range. Therefore, a methodology to determine the optimal wind output curtailment considering the system operation cost and DC voltage fluctuation is necessary.

B. LITERATURE REVIEW

This section introduces the primary control methods by the wind-side generation and HVDC systems. It is proved in [12] and [13] that the frequency controller of a multi-terminal VSC-HVDC system can improve the frequency stability. Fast frequency controllers by wind generation are discussed in [14], [15], [16], [17], and [18]. The coordinated control of both WPPs and generators for frequency regulation is proposed in [19]. The influence of the wind-side inertial response on improving the frequency dynamics is evaluated in [20]. Frequency control by WPPs connected via multi-terminal VSC-HVDC systems is investigated in [21]. Frequency controllers which utilize the energy of the DC grid and wind-side rotational energy are developed in [22] and [23].

Inertia emulation control (IEC) imitating the inertia response of generators is adopted in [24], [25], [26], [27], [28], and [29] for primary frequency control. A converter can control the active power flow to mimic the swing equation of synchronous generators. Virtual inertia can be provided by the converter to increase total system inertia. This has been evaluated as an effective method for power systems with low inertia. The benefits of the IEC implementation in HVDC systems are investigated in [12] and [30].

These methods are beneficial for improving the dynamic response and stability of power systems. In spite of this advantage, the reserve capacity of WPPs is necessary for wind-side-based frequency control. The output curtailment of WPPs is inevitable, which results in increased fuel operational costs. Nevertheless, none of the previous studies have mentioned a solution to determine the proper level of wind output curtailment considering this issue. In order to address this issue, our research group has formulated a frequency stability constrained-optimal power flow (FSC-OPF) [31]. The optimal wind output suppression ratio minimizing the fuel cost and satisfying the AC grid frequency stability constraint can be calculated.

Although previous studies have investigated the primary controllers of wind-side sources and HVDC systems, the following topics have not yet been assessed:

1) The relationship between the DC voltage fluctuation and wind-side reserve capacity considering the system operation costs has not been studied. Other studies have only discussed frequency stability improvements by wind-side generation and VSC-HVDC systems.
2) An integrated analysis of DC voltage considering both wind generation and the VSC-HVDC system is required since many large-scale WPPs are installed using VSC-HVDC systems. However, a methodology for an integrated analysis has not been suggested. In [32], the OPF formulation including the fast dynamics of turbine-governor systems is developed. It is proposed in [33] that frequency stability can be considered as a new constraint in the OPF analysis. Similarly, the DC grid voltage dynamics can be simultaneously affected by the controllers of wind generation and VSC-HVDC.

C. NOVEL CONTRIBUTION

The ratio of wind output suppression can be optimized in an OPF formulation. If the IEC is applied to a VSC-HVDC system, the DC grid voltage can fluctuate since active power is extracted from the DC grid side. In order to maintain a feasible DC voltage, the DC grid voltage constraint is included in the OPF analysis. The proposed methodology can be utilized by system operators to decide the proper level of wind output curtailment considering the DC grid voltage fluctuation and operation cost.

The major contributions of this article can be summarized as follows:

1) A new OPF formulation with DC grid voltage constraints is proposed. Not only the active power productions of synchronous generators, it can also determine the outputs of wind generation, and VSC-HVDC systems. As regards the wind output, the output curtailment ratio can be optimized to minimize the fuel costs of all generators.
2) The benefit of curtailed wind power production is discussed from the perspective of the DC voltage. The curtailed production of WPPs indicates that generators should produce more active power. This is not effective in minimizing the fuel cost objective function. On the other hand, reserve capacity can be secured by wind output curtailment. This can help maintain the DC grid voltage after a disturbance. If a DC voltage constraint is considered in the OPF formulation, the wind-side reserve capacity is beneficial for satisfying the DC voltage constraint. Therefore, the level of wind output curtailment should be optimized considering these aspects.
3) A sensitivity analysis of the curtailed wind power production is performed. The impacts of the DC voltage constraint and the system capacity on the curtailed wind output are studied.

This paper is composed as follows. A point-to-point VSC based HVDC system with the IEC controller is explained in Section II. The model of an aggregated wind turbine with output curtailment is illustrated in Section III. The OPF analysis to optimize the output suppression is proposed in

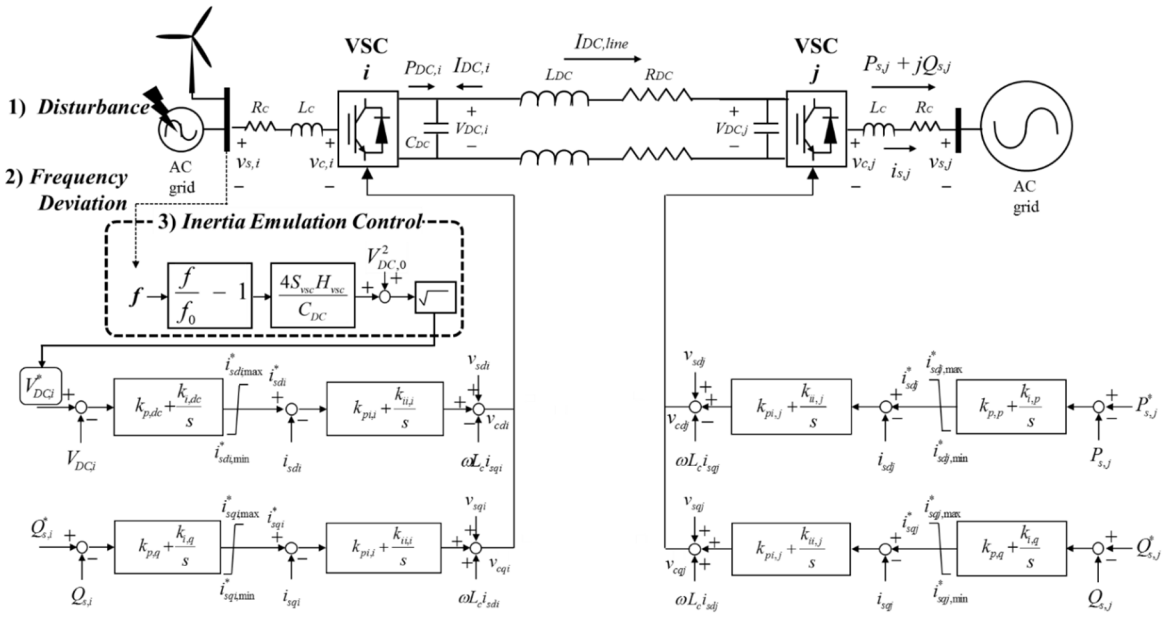

FIGURE 1. VSC-HVDC model with primary frequency support by IEC [31].

Section IV. Section V describes an integrated system model of AC/VSC-HVDC. The effectiveness of the proposed optimization method is validated based on the simulation results in Section VI.

II. VSC-HVDC MODEL

A. AVERAGE VALUE MODEL

A single-line diagram and the IEC controller of the VSC-HVDC model are shown in FIGURE 1 [31]. Modular multi-level converter (MMC) based topology with many sub-modules have been applied in recent VSC-HVDC projects. The average value model (AVM) of the MMC-based HVDC system in FIGURE 1 neglects the detailed switching behaviors of the sub-modules. The dynamic behaviors of an integrated AC/MMC-HVDC system can be represented by the AVM model with high accuracy and low computational burden [34], [35]. The AVM model explained in [31] is adopted.

Each bus is notated by either 'i' or 'j'. The DC grid bus voltage is regulated by the slack converter VSC i. VSC j regulates the output of the active power flow.

The VSC-HVDC system is connected to AC grid sides via point of common coupling (PCC) buses. As regards these connections, the resistive and inductive components of the AC transformers and filters are denoted by R_c and L_c respectively. The AC grid angular frequency is denoted by ω. The v_s and v_c voltage relationships in the synchronously rotating dq axis are represented by (1) and (2) respectively. i_{sd} and i_{sq} correspond to the outer vector current controllers' outputs.

Equation (3) indicates Kirchhoff's current law at DC grid bus i. V_{DC} and C_{DC} mean the DC bus voltage and the capacitance of the DC grid model respectively. I_{DC} and P_{DC} represent the current and active power supplied into the DC bus. The DC transmission line current is determined by (4) where $I_{DC,line}$ is the DC line current. Equations (5) and (6) correspond to the active and reactive power productions P_s and Q_s of VSC i respectively.

$$L_c \frac{di_{sdi}}{dt} = -R_c i_{sdi} + \omega L_c i_{sqi} + v_{cdi} - v_{sdi} \quad (1)$$

$$L_c \frac{di_{sqi}}{dt} = -R_c i_{sqi} - \omega L_c i_{sdi} + v_{cqi} - v_{sqi} \quad (2)$$

$$C_{DC} \frac{dV_{DC,i}}{dt} = -\frac{P_{DC,i}}{V_{DC,i}} + I_{DC,i} \quad (3)$$

$$L_{DC} \frac{dI_{DC,line}}{dt} = -R_{DC} I_{DC,line} + V_{DC,i} - V_{DC,j} \quad (4)$$

$$P_{s,i} = v_{sdi} i_{sdi} + v_{sqi} i_{sqi} \quad (5)$$

$$Q_{s,i} = v_{sqi} i_{sdi} - v_{sdi} i_{sqi} \quad (6)$$

B. PRIMARY FREQUENCY SUPPORT

Inertia emulation control (IEC) is adopted as the primary frequency controller in this paper. A detailed explanation of the IEC is provided in [12], [30], and [31]. The IEC controller adjusts the reference of the DC grid voltage V_{DC_ref}. The inertial dynamics of synchronous machines can be mimicked by this adjustment.

In general, the inertia constant value H of a conventional synchronous machine is expressed as (7) where the numerator corresponds to the kinetic energy of the generator at the synchronous speed ω_0 and S_G is the generator machine rating. The moment of inertia is represented by J. The notation 0 indicates the steady-state operation value.

In a similar manner, the inertia constant H_{vsc} provided by the IEC of a VSC can be defined in (8). The electromagnetic

energy stored in the DC grid capacitor C_{DC} is represented by the numerator. S_{vsc} indicates VSC converter ratings.

$$H = \frac{\frac{1}{2}J\omega_0^2}{S_G} \tag{7}$$

$$H_{vsc} = \frac{\frac{1}{2}C_{DC}V_{DC,0}^2}{S_{VSC}} \tag{8}$$

Equation (9) describes the rotational behavior of conventional synchronous generators. P_m and P_e represent the mechanical power input and electrical power output respectively. f and S stand for the system frequency in the AC grid and the generator power rating respectively. Equation (9) can be represented as (10) based on the approximation $f \approx f_0$.

$$\frac{2HS}{f_0^2} f \frac{df}{dt} = P_m - P_e \text{ [MW]} \tag{9}$$

$$\frac{2H}{f_0} \frac{df}{dt} = P_m - P_e \text{ [p.u.]} \tag{10}$$

If an analogy between generators and VSCs is introduced, the symbols f and H of a generator are replaced by the DC grid voltage V_{DC} and the virtual inertia H_{vsc} of the VSC-HVDC system in (11). The input and output active power values of the VSC converter are notated as P_{in} and P_{out} respectively. This implies that the adjustment of V_{DC} changes the active power flow of the VSC converter between the AC and DC grids.

$$\frac{C_{DC}V_{DC}}{S_{vsc}} \frac{dV_{DC}}{dt} = P_{in} - P_{out} \text{ [p.u.]} \tag{11}$$

The left sides of equations (10) and (11) can be equated from the active power perspective. As a result, equation (12) is obtained. This can also be expressed as (13) and (14).

If $V_{DC\_ref} = V_{DC}$, the DC grid voltage reference is given by (15). Equation (15) indicates that the new DC voltage reference $V_{DC,ref}$ (or $V_{DC}{}^*$) is determined based on the steady-state DC voltage value $V_{DC,0}$ and the ratio of the frequency fluctuation f / f_0. For example, an AC grid frequency drop after a disturbance results in a $V_{DC}{}^*$ reference reduction. This aims to release active power from the DC grid using a VSC converter to support the AC grid frequency.

$$\frac{2H_{vsc}}{f_0} \frac{df}{dt} = \frac{C_{DC}V_{DC}}{S_{vsc}} \frac{dV_{DC}}{dt} \tag{12}$$

$$\int_{f_0}^{f} \frac{2H_{vsc}}{f_0} df = \int_{V_{DC,0}}^{V_{DC}} \frac{C_{DC}V_{DC}}{S_{vsc}} dV_{DC} \tag{13}$$

$$\frac{2H_{vsc}}{f_0}(f - f_0) = \frac{C_{DC}}{2S_{vsc}}(V_{DC}^2 - V_{DC,0}^2) \tag{14}$$

$$V_{DC}^* = \sqrt{V_{DC,0}^2 + \frac{4S_{vsc}H_{vsc}}{C_{DC}}(\frac{f}{f_0} - 1)} \tag{15}$$

III. WIND TURBINE MODEL WITH OUTPUT CURTAILMENT

A. WIND TURBINE MODEL

The wind turbine model is described in FIGURE 2. The aggregated model with primary frequency support in [31] is simulated. The wind model has VSC converters in rotor and grid sides. In general, the response time of the converters is extremely fast. Hence, the active power P_{WT} of the wind model is assumed to follow its reference without any delay [21]. For the simplicity, the reactive power output of the wind model is not considered. The effect of the reactive power regulation will be covered in future works.

The dynamic characteristics of the wind model are expressed as (16)-(17). H_{WT} and ω_r denote the inertia constant and the rotational speed of the wind model respectively. $P_{m,WT}$ is the mechanical power input of the wind power plant.

$$2H_{WT}\omega_r \frac{d\omega_r}{dt} = P_{m,WT} - P_{WT} \text{ [p.u.]} \tag{16}$$

$$\frac{d\omega_r}{dt} = \frac{1}{2H_{WT}\omega_r}(P_{m,WT} - P_{WT}) \text{ [p.u.]} \tag{17}$$

The wind power plant power production in (18) is decided by the coefficient C_{WT} and rotational speed ω_r of a wind turbine. C_{WT} is determined by the characteristics of the wind turbine such as blade radius, wind speed, and rotor speed. The wind model can participate in the AC grid frequency control by implementing the controller in (19). The frequency f_{WF} at the point of common coupling bus is measured to obtain the adjustment of the active power output after a disturbance. The output of the wind model P_{WT} is composed of P_{MPPT} and P_f in (20) – (21).

$$P_{MPPT} = C_{WT}\omega_r^3 \tag{18}$$

$$P_f = k_f(f_{WT,0} - f_{WT}) \tag{19}$$

$$P_{WT} = P_{MPPT} + P_f \tag{20}$$

$$P_{WT} = C_{WT}\omega_r^3 + k_f(f_{WF,0} - f_{WF}) \tag{21}$$

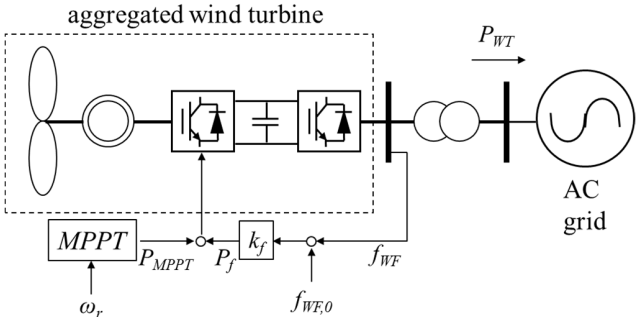

FIGURE 2. Aggregated wind turbine model [21], [31].

B. WIND OUTPUT CURTAILMENT

Wind output should be curtailed to secure the wind-side reserve capacity [36]. Rotor overspeed and pitch-angle-based methods can be implemented for the output curtailment [36], [37].

Compared to the MPPT curve operation, the wind power output is suppressed by the rotor-speed control by increasing the speed. The principle of the rotor overspeed control is plotted in FIGURE 3. If the MPPT curve operation

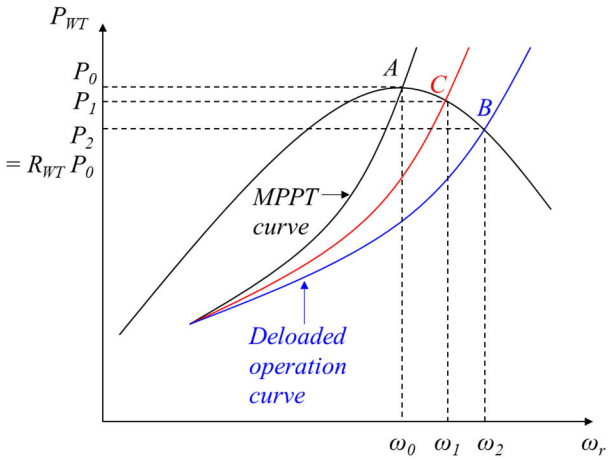

FIGURE 3. Overspeed control for output curtailment [31], [36].

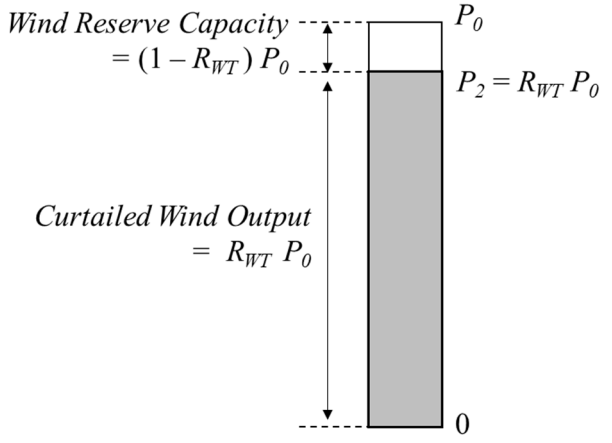

FIGURE 4. Wind-side reserve capacity by output curtailment.

point is A, the curtailed wind output curve corresponds to the blue line. Point B indicates the wind output suppression operation. Active power production is curtailed by (1 - R_{WT})P_0 in FIGURE 4 by increasing the rotor speed from ω_0 to ω_2. R_{WT} represents the ratio of the curtailed wind output to the rated wind output. When an active power deficit is measured, the wind power output increases from P_2 to P_1 by adjusting the rotor speed from ω_2 to ω_1 at point C.

With regard to the pitch-angle-based method, the angle is zero for a normal operation. The wind power output can be curtailed by increasing the pitch angle. This angle can be reduced to provide active power when an active power deficit is observed. The wind output adjustment range is larger than that of the rotor speed control method. Nevertheless, it is not suitable for low wind-speed conditions. In addition, it is not effective in achieving fast control performance considering the mechanical behavior. Hence, the rotor-speed-based method is implemented for the wind output curtailment in this paper.

IV. OPTIMAL POWER FLOW WITH DC VOLTAGE CONSTRAINT

A. OPF FORMULATION

This section presents the formulation of the OPF analysis with a DC voltage constraint for the integrated AC/VSC-HVDC systems. Based on the formulation in [31], dynamic DC voltage characteristics is incorporated as inequality constraints. The OPF is formulated as follows:

$$f_0(x_o, u_o) = \sum_{n \in G} (C_n + B_n P_n + A_n P_n^2) \tag{22}$$

$$g_o(x_o, u_o) = 0 \tag{23}$$

$$h_o(x_o, u_o) \leq 0 \tag{24}$$

$$h_k(x_k, u_k) \leq 0 \tag{25}$$

u and x denote the control and state variable vectors respectively. The objective function (22) consists of the sum of the generator fuel costs. A quadratic function of P_n with A_n, B_n, and C_n fuel cost coefficients is used for the fuel cost of generator n. The steady-state equality and inequality constraints g and h are considered in (23)-(24). After the disturbance k, the constraint (25) is applied.

In AC grid side, the balances of active power and reactive power at the bus j_AC are considered in (26)-(27) [38]. In DC grid side, the active power balance of the bus j_DC in (28) is formulated. P and Q notate the active and reactive power injections at a bus respectively.

$$P_{n,j} - P_{load,j} + P_{vsc,j} = P_{j\_AC} \tag{26}$$

$$Q_{n,j} - Q_{load,j} + Q_{vsc,j} = Q_{j\_AC} \tag{27}$$

$$P_{n,DC,j} - P_{DC\_load,j} + P_{vsc,DC,j} = P_{j\_DC} \tag{28}$$

The upper and lower operational restrictions of the system components are included in the inequality constraint. The notations '*min*' and '*max*' represent the minimum and maximum operation limits respectively. The production of active, reactive, and apparent power by generator n is restricted in (29) – (31). Similarly, the power output constraints of the VSC converter are represented in (32) – (34). The AC and DC bus voltage magnitudes V_{AC} and V_{DC} are constrained so as not to deviate above 0.1 *p.u.* from their nominal values in (35) and (36). The transmission line active power flow P_{line} and the tap transformer ratio R_{Tap} are limited by their respective rating values in (37) and (38) respectively.

$$P_n^{\min} \leq P_n \leq P_n^{\max} \tag{29}$$

$$Q_n^{\min} \leq Q_n \leq Q_n^{\max} \tag{30}$$

$$S_n^{\min} \leq S_n \leq S_n^{\max} \tag{31}$$

$$P_{vsc}^{\min} \leq P_{vsc} \leq P_{vsc}^{\max} \tag{32}$$

$$Q_{vsc}^{\min} \leq Q_{vsc} \leq Q_{vsc}^{\max} \tag{33}$$

$$S_{vsc}^{\min} \leq S_{vsc} \leq S_{vsc}^{\max} \tag{34}$$

$$V_{AC}^{\min} \leq V_{AC} \leq V_{AC}^{\max} \tag{35}$$

$$V_{DC}^{\min} \leq V_{DC} \leq V_{DC}^{\max} \tag{36}$$

$$P_{line}^{\min} \leq P_{line} \leq P_{line}^{\max} \tag{37}$$

$$R_{Tap}^{\min} \le R_{Tap} \le R_{Tap}^{\max} \tag{38}$$

The steady-state wind power output can be curtailed to supply the reserve capacity. When a disturbance occurs, the DC grid voltage deviation occurred by the IEC can be reduced by this wind-side reserve capacity. On the other hand, the output of the generators should increase to satisfy the power balance constraint (26). As a consequence, the fuel cost objective function (22) of generators increases, which is not desirable from an economic viewpoint. Thus, the wind output curtailment should be decided prudently.

In this paper, the wind output curtailment level is handled as a control variable in the OPF analysis. The optimal curtailment level can be obtained by this approach. The ratio of the curtailed wind output to the rated wind capacity is defined as R_{WT}. For example, R_{WT} is 0.9 when the wind output curtailment of a 500MW wind farm is 50MW. The lower limit ${R_{WT}}^{min}$ is decided considering the pitch angle control and the rotor-speed adjustment performance. If the deloaded wind operation is not necessary, the maximum value of the ratio ${R_{WT}}^{max}$ is one. This can be incorporated as an additional constraint in (39).

$$R_{WT}^{\min} \le R_{WT} \le R_{WT}^{\max} \tag{39}$$

After the disturbance k, the power balancing equations of the AC and DC systems (40) – (42) should be satisfied.

$$P_{n,j,k} - P_{load,j,k} + P_{vsc,j,k} = P_{j\_AC,k} \tag{40}$$

$$Q_{n,j,k} - Q_{load,j,k} + Q_{vsc,j,k} = Q_{j\_AC,k} \tag{41}$$

$$P_{n,DC,j,k} - P_{DC\_load,j,k} + P_{vsc,DC,j,k} = P_{j\_DC,k} \tag{42}$$

The frequency or rotational speed f_n of generator n is checked so as not to fluctuate above the criterion f_{range} in (43). In addition, the deviation of f_{COI} above f_{range} is forbidden in (44), where the frequency at the center of inertia f_{COI} is defined in (45) [39], [40].

$$f_n \le f_{n,0} \pm f_{range} \quad n = 1, 2, \cdots, G \tag{43}$$

$$f_{COI,k} \le f_{COI,0} \pm f_{range} \tag{44}$$

$$f_{COI} = \sum_{n \in G} \frac{f_n H_n}{H_n} \tag{45}$$

The IEC of the VSC-HVDC system in (15) results in a DC voltage reference fluctuation. Even if the IEC is helpful for the AC grid frequency regulation, an infeasibly large DC voltage deviation should be avoided. Hence, the DC voltage reference of the VSC slack is constrained in (46). It indicates the DC voltage reference after the disturbance k ${V_{DC,k}}^*$ should not deviate above the feasible range ${V_{DC,range}}^*$. Based on (15), the DC voltage reference constraint (46) can be defined as (47).

$$V_{DC,k}^* \le V_{DC,0} \pm V_{DC,range}^* \tag{46}$$

$$\sqrt{V_{DC,0}^2 + \frac{4 S_{vsc} H_{vsc}}{C_{DC}} \left(\frac{f}{f_0} - 1\right)} \le V_{DC,0} \pm V_{DC,range}^* \tag{47}$$

B. OPTIMIZATION ALGORITHM

A revised version of the differential evolution with the filtering-out process is adopted for the OPF analysis [31], [38]. In comparison with mathematical optimization methods, the dynamic characteristics of power system stability can be accurately incorporated by time-domain simulation using this evolutionary method.

The optimization algorithm is described in FIGURE 5. The set of parent control vector '*u_set*' composed of control vectors '*u*' is randomly initialized within the minimum and maximum values. Load flow analysis is carried out for each vector u to check its feasibility. If one of the constraints is

not satisfied, the control vector is classified as infeasible and a huge penalty value is imposed to its fitness function.

In order to check whether a control vector u satisfies the post-disturbance constraints (40) – (47), time-domain simulation should be conducted for all u vectors, which requires a huge computational burden. The principle of the filtering-out process is that the dynamic time-domain simulation is performed only for feasible u vectors [38]. When one of the post-disturbance constraints (40) – (47) is not satisfied, a penalty value 'α' is added to its fitness function. Instead of the time-domain simulation, the fitness value of the infeasible u vector is penalized by the filtering number 'β'. In order for the filtering out to be effective, the filtering penalty value β should be larger than the penalty α.

The set of trial vectors '*w_set*' is generated. The same process of the load flow analysis, time-domain simulation is applied to the w vectors.

The fitness values of each parent and trial vector are compared. The vector with the lower fitness function is selected by the evolutionary algorithm. The entire calculation procedure is repeated until the iteration number reaches the maximum trial limit K_{max}.

In this paper, the penalty values are determined as follows. The penalties for (26) – (39) violations and α are assigned as 100 times larger than the expected scale of the objective function value. Therefore, the control vector with no penalty is chosen in the selection step. As regards the penalty value β, it is 100 times larger than α so that a control vector with penalty β will never be selected. If more constraints should be considered by time-domain simulation, the ratio of β to α should also increase for effective filtering out.

V. POWER SYSTEM MODEL

The integrated AC/VSC-HVDC model [31] is shown in FIGURE 6. The fuel cost coefficients in [41] are used for the simulation. Static constant power load model is adopted for all AC grid loads.

An aggregated wind turbine model is placed near G7. The fuel cost coefficients of the wind farm are zero. The output of the wind farm can be curtailed to obtain the reserve capacity. The maximum wind output curtailment ratio is 10% in this paper. For instance, a 500MW wind farm can provide 50MW of reserve capacity to support the DC voltage after a

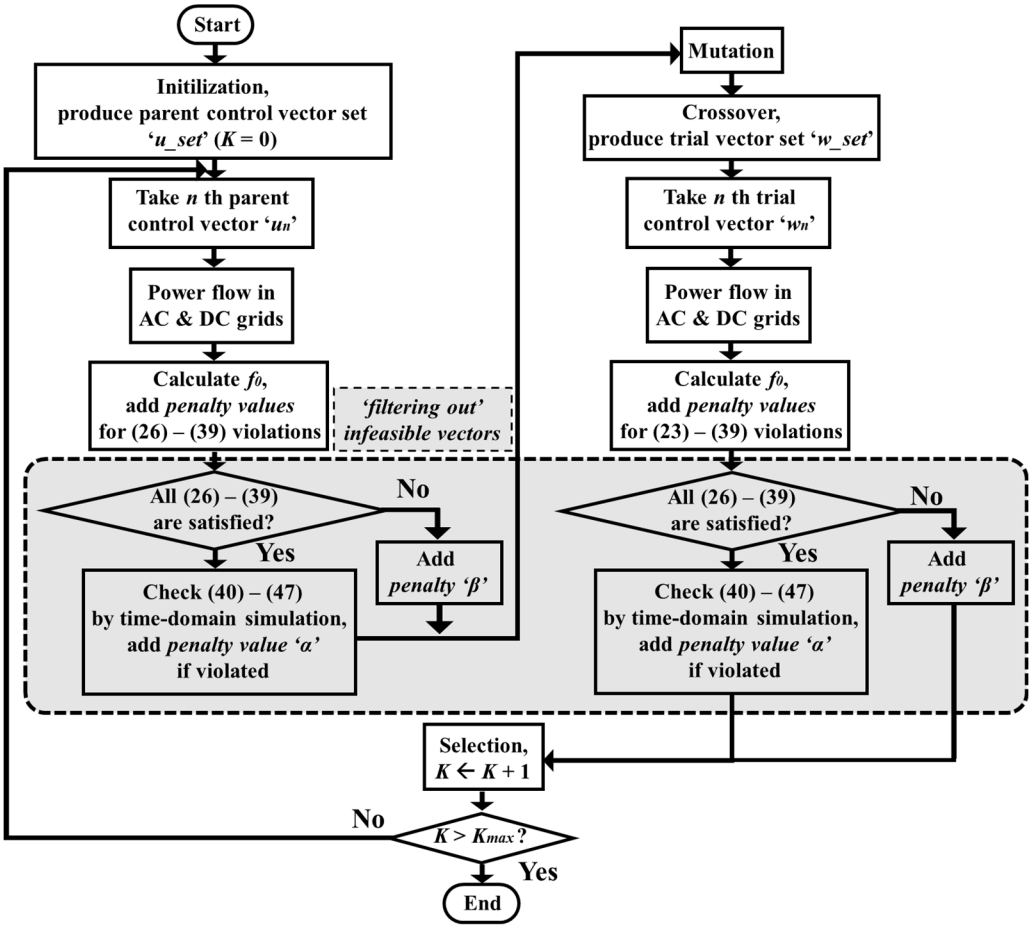

FIGURE 5. Optimization algorithm using differential evolution [31].

disturbance. The inertia value H_{WT} of the wind generation is 4 seconds.

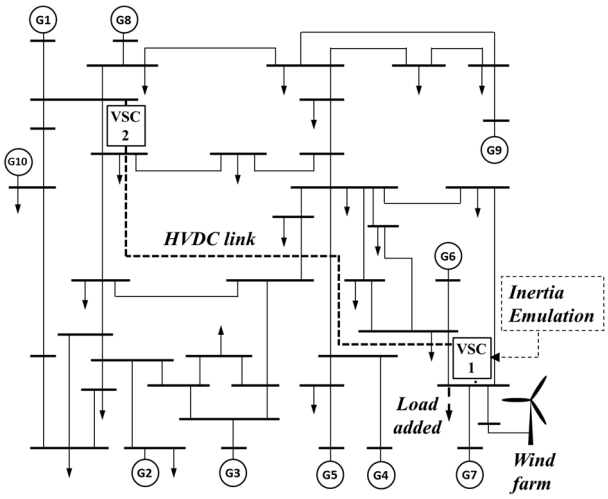

FIGURE 6. Integrated AC/VSC-HVDC system model with wind farm.

A load connection near G7 is considered as the disturbance. The power consumption of the connected load is 500MW with a 0.958 lagging power factor. All ten generators except G10 have their AVR [42] and GOV [32] models which are described in the Appendix.

The nominal DC grid voltage level is 500kV. VSC 1 is the slack converter which controls the DC grid voltage. The IEC is applied to the slack converter VSC 1. The DC voltage reference of the slack converter is 1.0 *p.u.* during normal operation. When a frequency deviation is observed, this DC voltage reference can be adjusted by the IEC. VSC 2 is assigned to maintain the VSC active power production. The VSC-HVDC control parameters are listed in TABLE 7 in the Appendix. The parameters are determined by the preliminary tuning process.

The proper DC capacitor rating C_{DC} is important for effective IEC performance. A low C_{DC} rating leads to infeasibly huge deviations of the DC voltages after the IEC is activated. An excessively high C_{DC} rating is not economical considering the investment cost. The explanations to determine feasible C_{DC} are provided in [12], [30], and [43]. Based on

these preliminary approaches, C_{DC} rating is $2ms$ of each VSC capacity in this paper.

VI. RESULTS AND DISCUSSION

A. REDUCED DC VOLTAGE FLUCTUATION BY WIND OUTPUT CURTAILMENT

This section discusses the time-domain simulation results to validate the effect of the wind output curtailment on the DC grid voltage. Three cases with H_{vsc} from 0.1 $\sim$ 0.3 seconds are considered to reveal the impact of the IEC.

The installed capacities of the VSC-HVDC system and the wind farm are 1000MVA and 600MW respectively. As the disturbance, the load is connected at $t = 1$ second.

The speed curve of generator G7 is shown in FIGURE 7. When the H_{vsc} value of the slack VSC is 0.1 s, the nadir value is 59.9Hz. When a frequency drop is detected, the VSC slack can supply active power to the AC grid by activating the IEC control. The frequency deviation decreases as the H_{vsc} value increases in FIGURE 7.

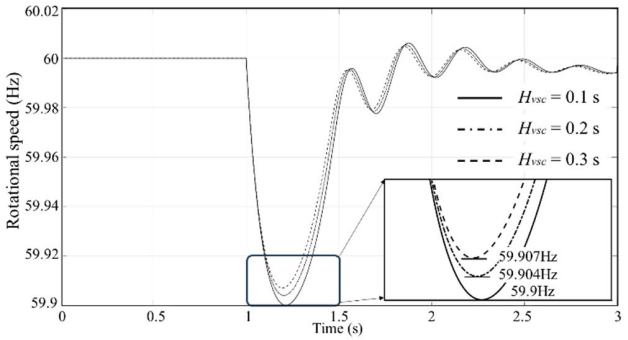

FIGURE 7. Rotational speed trajectories of generator G7.

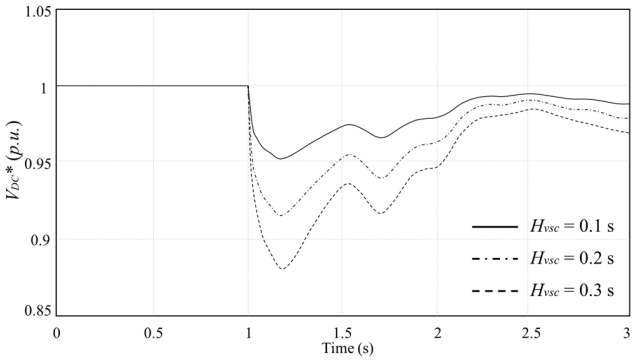

FIGURE 8. DC voltage reference $V_{DC}*$ of VSC 1.

On the other hand, the IEC yields the deviation of the DC voltage reference since the active power should be extracted from the DC grid side. The DC voltage reference deviation increases as the H_{vsc} value increases. The relationship between the DC voltage reference deviation and H_{vsc} is shown in FIGURE 8.

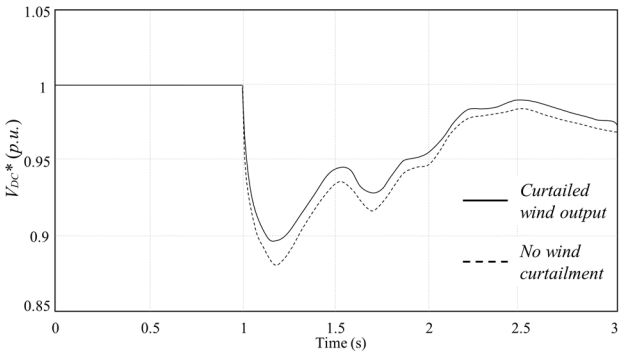

FIGURE 9. Impact of wind output curtailment on DC voltage reference $V_{DC}*$ (H_{vsc} = 0.3 s).

One of the novel points of this paper is to maintain the DC voltage reference deviation and satisfy the constraint (47) using the wind-side reserve capacity. If the steady-state production of a wind model is reduced to obtain the reserve capacity, active power can be supplied from the wind generation after a disturbance. In other words, system operators can substitute the wind-side frequency regulation for the IEC of a VSC-HVDC. Consequently, the DC voltage reference deviation triggered by the IEC can be reduced if the wind-side reserve capacity is available. The benefit of the curtailed wind output in reducing the DC grid voltage reference deviation can be seen in FIGURE 9 where H_{vsc} is fixed to be 0.3 s.

B. SENSITIVITY ANALYSIS ON DC VOLTAGE CONSTRAINTS

The OPF analysis is performed under various DC voltage constraints. The optimal curtailed wind operation ratio R_{WT} results are listed in Table 1. When the OPF solution cannot be found, such cases are notated by 'X'. The capacities of the VSC-HVDC system and the wind farm are 1000MVA and 600MW respectively. Different H_{vsc} values from 0.1 to 0.3 seconds are tested. Regarding the frequency constraints in (43) and (44), the deviation range f_{range} is 0.1Hz.

When the DC voltage deviation constraint $V_{DC}^{*}{}_{,range}$ is 0.14 $p.u.$, the optimal wind operation ratio is 0.972 if H_{vsc} is either 0.1 s or 0.2 s. In other words, it can be inferred that 2.8% of the rated wind output is needed as the reserve capacity considering the DC voltage constraint. The DC voltage fluctuation increases when H_{vsc} is 0.3 s. In this case, more wind-side reserve capacity is required. Therefore, the operation ratio is reduced by 0.007.

When H_{vsc} is 0.1 s, the DC voltage fluctuation is not significant compared to the cases with higher H_{vsc} values. Thus, the optimal wind operation ratio R_{WT} is the same for all DC voltage constraint scenarios in Table 1.

On the contrary, the optimal R_{WT} ratio is 0.940 when H_{vsc} is 0.2 s and $V_{DC}^{*}{}_{,range}$ is 0.09 $p.u.$. In order to comply with the DC voltage constraint, 6% of the rated wind production is required. If $V_{DC}^{*}{}_{,range}$ is lower than 0.09 $p.u.$, no OPF solution is found.

The results when H_{vsc} is 0.3 s show a similar tendency. The optimal R_{WT} ratio value decreases as the DC voltage constraint $V_{DC}{}^{*}_{,range}$ becomes stricter. When $V_{DC}{}^{*}_{,range}$ is less than 0.12 *p.u.*, OPF solutions are not obtained.

The results can be summarized as follows. The IEC control of the VSC-HVDC system results in a DC voltage reference deviation. If the DC grid voltage constraint is considered, a curtailed wind output operation R_{WT} is required. Moreover, the DC voltage deviation increases as the H_{vsc} value increases. The optimal ratio R_{WT} should be reduced in such cases.

C. SENSITIVITY ANALYSIS ON WIND MODEL CAPACITY

The cases under various wind farm capacities are simulated. A 1000MVA VSC-HVDC system is installed. The frequency deviation range f_{range} in (43) and (44) is 0.1Hz.

TABLE 1. Curtailed wind operation ratio R_{WT} with different DC voltage constraints.

$V_{DC}{}^{*}_{,range}$ (*p.u.*)	H_{vsc} (sec)		
	0.1	0.2	0.3
0.14	0.972	0.972	0.965
0.13			0.946
0.12			0.938
0.11			X
0.10			
0.09		0.940	
0.08		X	
0.07			
0.06			
0.05			

In this section, the OPF analysis is performed in two separate stages. In the first stage, the minimum deviation range of the DC voltage reference constraint $V_{DC}{}^{*}_{,range}$ is calculated in Table 2. This aims to find the strictest DC voltage constraint for each wind capacity scenario. For instance, the result of 0.095 implies that when the wind farm capacity is 300MW, the minimum DC voltage reference deviation is 0.095 *p.u.*. The OPF solution does not exist if $V_{DC}{}^{*}_{,range}$ is 0.094 *p.u.*. Hence, the results in Table 2 correspond to the strictest constraints from the viewpoint of DC voltage. Based on these results, the optimal wind operation ratio values R_{WT} are calculated in the second stage in Table 3.

First of all, a feasible solution is not found with $H_{vsc} = 0.1$ s when a 300MW wind farm is installed. The frequency constraint (43) of G7 cannot be satisfied since $H_{vsc} = 0.1$ s is too low. In such a low H_{vsc} scenario, the primary frequency support of the wind-side generation is required. However, the wind-side reserve capacity cannot be secured due to the lack of wind capacity.

Unlike the case with a 300MW wind farm, the wind-side reserve capacity can be provided when the wind capacity is 400MW. The corresponding minimum deviation range $V_{DC}{}^{*}_{,range}$ in Table 2 is 0.047 *p.u.*. This DC voltage deviation can be reduced by 0.003 *p.u.* if the wind farm capacity is increased by 200MW.

When H_{vsc} is higher than 0.2 s, feasible OPF solutions can be obtained for the 300MW wind farm cases. The minimum range of $V_{DC}{}^{*}_{,range}$ is 0.095 *p.u.* with $H_{vsc} = 0.2$ s. The fluctuation of $V_{DC}{}^{*}_{,range}$ is 0.130 *p.u.* with $H_{vsc} = 0.3$ s since more active power is extracted from the DC grid by the IEC. The minimum range of $V_{DC}{}^{*}_{,range}$ can be reduced if the wind farm capacity increases. For example, the minimum deviation of the DC voltage reference is 0.081 *p.u.* with $H_{vsc} = 0.2$ s when the wind farm capacity is 600MW. Similarly, the lowest DC voltage deviation of 0.113 *p.u.* is observed among all the wind capacity scenarios when H_{vsc} is 0.3 s.

The results in Table 2 can be concluded as follows. As the wind farm capacity increases, the available wind-side reserve capacity also increases. Hence, stricter DC voltage constraints can be imposed.

TABLE 2. Minimum value of DC voltage reference constraint $V_{DC}{}^{*}_{,range}$ with different wind capacity.

Wind capacity (MW)	H_{vsc} (sec)		
	0.1	0.2	0.3
300	X	0.095	0.130
400	0.047	0.087	0.122
600	0.044	0.081	0.113

TABLE 3. Curtailed wind operation ratio R_{WT} with different wind capacity.

Wind capacity (MW)	H_{vsc} (sec)		
	0.1	0.2	0.3
300	X	0.927	0.933
400	0.940	0.941	0.941
600	0.945	0.955	0.955

For the scenario with a 300MW wind farm, the optimal wind operation ratio R_{WT} is 0.927 for $H_{vsc} = 0.2$ s in Table 3 When $V_{DC}{}^{*}_{,range}$ of the DC voltage constraint is 0.095 in Table 2. When H_{vsc} is 0.3 s, the minimum DC voltage deviation range $V_{DC}{}^{*}_{,range}$ increases. This means the wind-side reserve capacity can be reduced. As a consequence, a higher R_{WT} ratio value of 0.933 is obtained for $H_{vsc} = 0.3$ s in Table 3. A similar tendency can be seen in 600MW wind capacity scenarios. Compared to the R_{WT} result with $H_{vsc} = 0.1$ s, a higher optimal ratio of 0.955 is obtained when H_{vsc} is either 0.2 s or 0.3 s. The R_{WT} ratio differences for 400MW wind capacity are relatively insignificant. In this case, the optimal R_{WT} ratio can be applied to all the three H_{vsc} cases.

D. SENSITIVITY ANALYSIS ON HVDC CAPACITY

Various VSC-HVDC system capacity scenarios are examined in this section. The wind farm capacity is 600MW. The inertia constant H_{vsc} of VSC 1 is 0.2 seconds. f_{range} of the frequency constraint is 0.1Hz.

As explained in the previous section, the minimum deviation range of the DC voltage $V_{DC}{}^{*}_{,range}$ is calculated for each case. The optimal wind operation ratio R_{WT} is determined based on this strictest DC voltage constraint $V_{DC}{}^{*}_{,range}$. The minimum DC voltage reference constraints $V_{DC}{}^{*}_{,range}$ and the corresponding R_{WT} values are listed in Table 4.

TABLE 4. Curtailed wind operation ratio R_{WT} and minimum value of DC voltage reference constraint $V_{DC}{}^{*}_{,range}$ with various HVDC system capacities.

HVDC capacity (MVA)	*minimum of* $V_{DC}{}^{*}_{,range}$ *(p.u.)*	R_{WT}
400	X	
600	0.120	0.916
800	0.098	0.935
1000	0.081	0.948

Considering the frequency stability constraint (43), the 400MVA HVDC system is not sufficient to offer reserve capacity. Therefore, an OPF solution cannot be obtained. If the 600MVA VSC-HVDC system is installed, the minimum value of $V_{DC}{}^{*}_{,range}$ is 0.120 *p.u.* and the corresponding wind operation ratio R_{WT} is 0.916. As the HVDC capacity increases, the reserve capacity from the HVDC side also increases. Thus, the wind-side reserve capacity can be reduced. As a result, the optimal wind operation ratio R_{WT} increases and the minimum value of $V_{DC}{}^{*}_{,range}$ decreases as the HVDC system capacity increases. Therefore, the lowest wind output curtailment and the strictest $V_{DC}{}^{*}_{,range}$ constraint 0.081 *p.u.* are calculated for a 1000MVA HVDC system.

VII. CONCLUSION

The methodology for wind power output curtailment optimization is proposed. It is based on the OPF analysis in a hybrid AC/VSC-HVDC system with inertia emulation control. The limitation of DC grid voltage range is included as an additional constraint to maintain the DC grid voltage deviation within a feasible range. If the curtailed wind production is considered, the IEC of the VSC-HVDC system can be substituted for the wind-side frequency regulation. This contributes to the reduced DC grid voltage deviation to satisfy the DC voltage constraint. It is revealed in the sensitivity analysis that a strict DC voltage constraint leads to a large wind output curtailment. The curtailed wind operation ratio increases as the wind power plant capacity increases. If the capacity of a VSC-HVDC system is sufficient to supply the reserve capacity, the curtailment ratio of wind production decreases.

The role of reactive power regulation by the wind turbine model will be studied in the future. In addition, a distributed controller based on a multi-terminal HVDC configuration will be implemented. On top of that, the results with multiple wind farms and different control system parameters can be discussed. The proposed methodology can be applied to other power system models considering different disturbance types and locations.

APPENDIX

See Figs. 10, 11, and Tables 5–7.

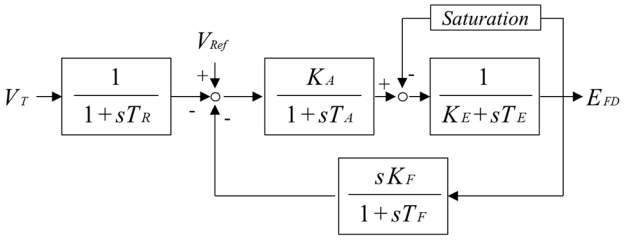

FIGURE 10. IEEE Type 1 excitation model [42].

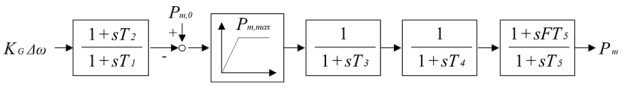

FIGURE 11. Turbine-governor model [32].

TABLE 5. Parameters of AVR model.

	T_R (s)	K_A	T_A (s)	K_E	T_E (s)	K_F	T_F (s)
G1	1	200	0.358	1	0.004	0.0529	1
G2	1	400	0.0200	1	0.942	0.0300	1
G3	1	400	0.0200	1	0.942	0.0300	1
G4	1	400	0.0200	1	0.942	0.0300	1
G5	1	400	0.0200	1	0.942	0.0300	1
G6	1	400	0.0200	1	0.942	0.0300	1
G7	1	400	0.0200	1	0.942	0.0300	1
G8	1	400	0.0200	1	0.942	0.0300	1
G9	1	50	0.0600	-0.0393	0.440	0.0700	1

TABLE 6. Parameters of turbine-governor model.

	K_G	T_1 (s)	T_2 (s)	T_3 (s)	T_4 (s)	T_5 (s)	F
G1	20	0.2	0.4	0.3	0	10	0.3
G2	20	0.2	0.4	0.3	0	10	0.3
G3	20	0.2	0.4	0.3	0	10	0.3
G4	20	0.2	0.4	0.3	0	10	0.3
G5	20	0.2	0.4	0.3	0	10	0.3
G6	20	0.2	0.4	0.3	0	10	0.3
G7	20	0.2	0.4	0.3	0	10	0.3
G8	20	0.2	0.4	0.3	0	10	0.3
G9	20	0.2	0.4	0.3	0	10	0.3

TABLE 7. Parameters of VSC-HVDC control system.

System	Item	Value [*p.u.*]
PI Controller	Outer active power controller ($k_{p,p}$, $k_{i,p}$)	(1, 2)
	Outer reactive power controller ($k_{p,q}$, $k_{i,q}$)	(1, 2)
	Outer DC voltage controller ($k_{p,dc}$, $k_{i,dc}$)	(4, 8)
	Inner current controller (k_{pi} , k_{ii})	(1, 20)

REFERENCES

[1] L. Xu, L. Yao, and C. Sasse, "Grid integration of large DFIG-based wind farms using VSC transmission," *IEEE Trans. Power Syst.*, vol. 22, no. 3, pp. 976–984, Aug. 2007.

[2] E. Pierri, O. Binder, N. G. A. Hemdan, and M. Kurrat, "Challenges and opportunities for a European HVDC grid," *Renew. Sustain. Energy Rev.*, vol. 70, pp. 427–456, Apr. 2017.

[3] J. Liu, W. Yao, J. Wen, J. Fang, L. Jiang, H. He, and S. Cheng, "Impact of power grid strength and PLL parameters on stability of grid-connected DFIG wind farm," *IEEE Trans. Sustain. Energy*, vol. 11, no. 1, pp. 545–557, Jan. 2020.

[4] Y. Li, G. Tang, T. An, H. Pang, P. Wang, J. Yang, Y. Wu, and Z. He, "Power compensation control for interconnection of weak power systems by VSC-HVDC," *IEEE Trans. Power Del.*, vol. 32, no. 4, pp. 1964–1974, Aug. 2017.

[5] G.-S. Lee, D.-H. Kwon, Y.-K. Kim, and S.-I. Moon, "A new communication-free grid frequency and AC voltage control of hybrid LCC-VSC-HVDC systems for offshore wind farm integration," *IEEE Trans. Power Syst.*, vol. 38, no. 2, pp. 1309–1321, Mar. 2023.

[6] Y. Zhang and A. M. Gole, "Quantifying the contribution of dynamic reactive power compensators on system strength at LCC-HVdc converter terminals," *IEEE Trans. Power Del.*, vol. 37, no. 1, pp. 449–457, Feb. 2022.

[7] H. Liu and Z. Chen, "Contribution of VSC-HVDC to frequency regulation of power systems with offshore wind generation," *IEEE Trans. Energy Convers.*, vol. 30, no. 3, pp. 918–926, Sep. 2015.

[8] Y. Wang, N. Zhang, C. Kang, M. Miao, R. Shi, and Q. Xia, "An efficient approach to power system uncertainty analysis with high-dimensional dependencies," *IEEE Trans. Power Syst.*, vol. 33, no. 3, pp. 2984–2994, May 2018.

[9] J. Li, S. Wang, L. Ye, and J. Fang, "A coordinated dispatch method with pumped-storage and battery-storage for compensating the variation of wind power," *Protection Control Modern Power Syst.*, vol. 3, no. 1, pp. 21–34, Dec. 2018.

[10] Y. Huang, X. Yuan, J. Hu, P. Zhou, and D. Wang, "DC-bus voltage control stability affected by AC-bus voltage control in VSCs connected to weak AC grids," *IEEE J. Emerg. Sel. Topics Power Electron.*, vol. 4, no. 2, pp. 445–458, Jun. 2016.

[11] A. Raza, A. Akhtar, M. Jamil, G. Abbas, S. O. Gilani, L. Yuchao, M. N. Khan, T. Izhar, X. Dianguo, and B. W. Williams, "A protection scheme for multi-terminal VSC-HVDC transmission systems," *IEEE Access*, vol. 6, pp. 3159–3166, 2018.

[12] J. Zhu, C. D. Booth, G. P. Adam, A. J. Roscoe, and C. G. Bright, "Inertia emulation control strategy for VSC-HVDC transmission systems," *IEEE Trans. Power Syst.*, vol. 28, no. 2, pp. 1277–1287, May 2013.

[13] O. D. Adeuyi, M. Cheah-Mane, J. Liang, and N. Jenkins, "Fast frequency response from offshore multiterminal VSC–HVDC schemes," *IEEE Trans. Power Del.*, vol. 32, no. 6, pp. 2442–2452, Dec. 2017.

[14] L. Fan, Z. Miao, and D. Osborn, "Wind farms with HVDC delivery in load frequency control," *IEEE Trans. Power Syst.*, vol. 24, no. 4, pp. 1894–1895, Nov. 2009.

[15] Y. Phulpin, "Communication-free inertia and frequency control for wind generators connected by an HVDC-link," *IEEE Trans. Power Syst.*, vol. 27, no. 2, pp. 1136–1137, May 2012.

[16] M. M. Kabsha and Z. H. Rather, "A new control scheme for fast frequency support from HVDC connected offshore wind farm in low-inertia system," *IEEE Trans. Sustain. Energy*, vol. 11, no. 3, pp. 1829–1837, Jul. 2020.

[17] G.-S. Lee, D.-H. Kwon, S.-I. Moon, and P.-I. Hwang, "A coordinated control strategy for LCC HVDC systems for frequency support with suppression of AC voltage fluctuations," *IEEE Trans. Power Syst.*, vol. 35, no. 4, pp. 2804–2815, Jul. 2020.

[18] D. Yang, J. Kim, Y. C. Kang, E. Muljadi, N. Zhang, J. Hong, S.-H. Song, and T. Zheng, "Temporary frequency support of a DFIG for high wind power penetration," *IEEE Trans. Power Syst.*, vol. 33, no. 3, pp. 3428–3437, May 2018.

[19] M. Sun, Y. Sun, L. Chen, Z. Zou, Y. Min, R. Liu, F. Xu, and Y. Wu, "Novel temporary frequency support control strategy of wind turbine generator considering coordination with synchronous generator," *IEEE Trans. Sustain. Energy*, vol. 13, no. 2, pp. 1011–1020, Apr. 2022.

[20] Z. Chu, U. Markovic, G. Hug, and F. Teng, "Towards optimal system scheduling with synthetic inertia provision from wind turbines," *IEEE Trans. Power Syst.*, vol. 35, no. 5, pp. 4056–4066, Sep. 2020.

[21] M. Mehrabankhomartash, M. Saeedifard, and A. Yazdani, "Adjustable wind farm frequency support through multi-terminal HVDC grids," *IEEE Trans. Sustain. Energy*, vol. 12, no. 2, pp. 1461–1472, Apr. 2021.

[22] Y. Li, Z. Zhang, Y. Yang, Y. Li, H. Chen, and Z. Xu, "Coordinated control of wind farm and VSC–HVDC system using capacitor energy and kinetic energy to improve inertia level of power systems," *Int. J. Electr. Power Energy Syst.*, vol. 59, pp. 79–92, Jul. 2014.

[23] A. Junyent-Ferr, Y. Pipelzadeh, and T. C. Green, "Blending HVDC-link energy storage and offshore wind turbine inertia for fast frequency response," *IEEE Trans. Sustain. Energy*, vol. 6, no. 3, pp. 1059–1066, Jul. 2015.

[24] Q.-C. Zhong and G. Weiss, "Synchronverters: Inverters that mimic synchronous generators," *IEEE Trans. Ind. Electron.*, vol. 58, no. 4, pp. 1259–1267, Apr. 2011.

[25] H. Bevrani, T. Ise, and Y. Miura, "Virtual synchronous generators: A survey and new perspectives," *Int. J. Electr. Power Energy Syst.*, vol. 54, pp. 244–254, Jan. 2014.

[26] S. D'Arco and J. A. Suul, "Virtual synchronous machines—Classification of implementations and analysis of equivalence to droop controllers for microgrids," in *Proc. IEEE Grenoble Conf.*, Grenoble, France, Jun. 2013, pp. 1–7.

[27] A. Tayyebi, Z. Miletic, F. Dorfler, F. Kupzog, and W. Hribernik, "Grid-forming converters—Inevitability, control strategies and challenges in future grid applications," in *Proc. Int. Conf. Electr. Distrib. (CIRED)*, Ljubljana, Slovenia, 2018.

[28] V. Karapanos, S. de Haan, and K. Zwetsloot, "Real time simulation of a power system with VSG hardware in the loop," in *Proc. IECON 37th Annu. Conf. IEEE Ind. Electron. Soc.*, Melbourne, VIC, Australia, Nov. 2011, pp. 3748–3754.

[29] M. Torres and L. A. C. Lopes, "Virtual synchronous generator: A control strategy to improve dynamic frequency control in autonomous power systems," *Energy Power Eng.*, vol. 5, no. 2, pp. 32–38, 2013.

[30] Z. Shen, J. Zhu, L. Ge, S. Bu, J. Zhao, C. Y. Chung, X. Li, and C. Wang, "Variable-inertia emulation control scheme for VSC-HVDC transmission systems," *IEEE Trans. Power Syst.*, vol. 37, no. 1, pp. 629–639, Jan. 2022.

[31] S. Kim, "Analysis of deloaded wind power in hybrid AC/HVDC systems by frequency stability constrained optimal power flow," *IEEE Access*, vol. 11, pp. 104441–104451, 2023, doi: 10.1109/ACCESS.2023.3318598.

[32] X. Zhao, H. Wei, J. Qi, P. Li, and X. Bai, "Frequency stability constrained optimal power flow incorporating differential algebraic equations of governor dynamics," *IEEE Trans. Power Syst.*, vol. 36, no. 3, pp. 1666–1676, May 2021.

[33] S. Kim, "A novel preventive frequency stability constrained OPF considering wind power fluctuation," in *Proc. IEEE PES Innov. Smart Grid Technol. Asia (ISGT Asia)*, Singapore, Nov. 2022, pp. 96–100.

[34] H. Saad, J. Peralta, S. Dennetière, J. Mahseredjian, J. Jatskevich, J. A. Martinez, A. Davoudi, M. Saeedifard, V. Sood, X. Wang, J. Cano, and A. Mehrizi-Sani, "Dynamic averaged and simplified models for MMC-based HVDC transmission systems," *IEEE Trans. Power Del.*, vol. 28, no. 3, pp. 1723–1730, Jul. 2013.

[35] J. Xu, A. M. Gole, and C. Zhao, "The use of averaged-value model of modular multilevel converter in DC grid," *IEEE Trans. Power Del.*, vol. 30, no. 2, pp. 519–528, Apr. 2015.

[36] X. Zhang, Y. Chen, Y. Wang, X. Zha, S. Yue, X. Cheng, and L. Gao, "Deloading power coordinated distribution method for frequency regulation by wind farms considering wind speed differences," *IEEE Access*, vol. 7, pp. 122573–122582, 2019.

[37] H. Luo, Z. Hu, H. Zhang, and H. Chen, "Coordinated active power control strategy for deloaded wind turbines to improve regulation performance in AGC," *IEEE Trans. Power Syst.*, vol. 34, no. 1, pp. 98–108, Jan. 2019.
[38] S. Kim, A. Yokoyama, Y. Takaguchi, T. Takano, K. Mori, and Y. Izui, "Transient stability constrained optimal power flow in mixed AC/multi-terminal VSC HVDC system," *IEEJ Trans. Electr. Electron. Eng.*, vol. 15, no. 10, pp. 1436–1447, Oct. 2020.
[39] C. Li, Y. Wu, Y. Sun, H. Zhang, Y. Liu, Y. Liu, and V. Terzija, "Continuous under-frequency load shedding scheme for power system adaptive frequency control," *IEEE Trans. Power Syst.*, vol. 35, no. 2, pp. 950–961, Mar. 2020.
[40] A. Ademola-Idowu and B. Zhang, "Frequency stability using MPC-based inverter power control in low-inertia power systems," *IEEE Trans. Power Syst.*, vol. 36, no. 2, pp. 1628–1637, Mar. 2021.
[41] T. B. Nguyen and M. A. Pai, "Dynamic security-constrained rescheduling of power systems using trajectory sensitivities," *IEEE Trans. Power Syst.*, vol. 18, no. 2, pp. 848–854, May 2003.
[42] P. Demetriou, M. Asprou, J. Quiros-Tortos, and E. Kyriakides, "Dynamic IEEE test systems for transient analysis," *IEEE Syst. J.*, vol. 11, no. 4, pp. 2108–2117, Dec. 2017.
[43] C.-H. Lin and Y.-K. Wu, "Overview of frequency-control technologies for a VSC-HVDC-integrated wind farm," *IEEE Access*, vol. 9, pp. 112893–112921, 2021.

SANGWON KIM (Member, IEEE) received the B.E. degree in electronic and electrical engineering from Sungkyunkwan University, Suwon, Republic of Korea, in 2015, and the M.E. and Dr.Eng. degrees in electrical engineering and information systems from The University of Tokyo, Japan, in 2017 and 2020, respectively. He was a Staff Engineer with the Global Manufacturing and Infrastructure Department, Samsung Electronics, South Korea, from 2020 to 2022. He is currently an Assistant Professor with the University of Ulsan, Ulsan, South Korea. His research interests include power system operation and stability analysis, including HVDC systems and renewable energy integration.